Materials LAB

RESEARCH ARTICLE

Materials Lab 2024, 3, 240007

3D-printing of patterned Zn anodes toward dendrite-free zinc ion batteries

Li Zeng[1], Yiyu Fang[1], Dan Luo[1], Dayue Du[1], Sijiang Hu[2], Hanna He[1*] and Chuhong Zhang[1*]

3D Zn anodes, boasting a high specific surface area to reduce the local current density, have emerged as promising electrodes for dendrite-free Zn-ion batteries (ZIBs). Despite their potential, the impact of diverse topological structures of Zn anodes on Zn deposition behavior within these electrodes remains poorly understood. To elucidate this relationship, this study employed direct ink writing technology to 3D print Zn anodes with four distinct topological configurations. The 3D array Zn anode featured with an angle between two connected printing strips of 180° (3DP-180) stood out for the fewest electrode joint points among these four anodes, migrating the tip effect and facilitating uniform electric field/ion distribution, which in turn promoted even Zn deposition and effectively suppressed Zn dendrites. The 3DP-180 array anode demonstrated a notably low nucleation overpotential of 27.2 mV, indicating a superior capacity for Zn nucleation and uniform Zn deposition. Moreover, symmetrical cell assembled with 3DP-180 array anode achieved 800 hours of continuous cycling without degradation at a current density of 1 mA cm^{-2} and a capacity of 0.5 mAh cm^{-2}. These results highlight the improved cycle lifespan afforded by the superior structural design of Zn anodes, offering valuable insights to inform the development of next-generation durable and safe ZIBs.

Aqueous metal batteries, utilizing water as the electrolyte, are emerging as promising energy storage systems. Among these, Zn-ion Batteries (ZIBs) have attracted significant attention due to the abundant reserves and high electrochemical activity of metallic Zn[1–3]. These characteristics endow ZIBs with high safety and suitability for large-scale energy storage. However, the growth of Zn dendrites and side reactions of Zn anodes lead to poor cycle stability of ZIBs, which severely restricts their commercial viability[4–5]. Zn dendrites pose a significant risk as they potentially pierce the separator, causing internal short circuits[6]. The formation of these dendrites is primarily influenced by uneven electric fields and ion concentrations. During the Zn deposition process, Zn^{2+} is driven by the electric field to the electrode-electrolyte interface, where ions nucleate on the collector surface after surmounting nucleation energy barrier[7–8]. A lower nucleation energy barrier generally facilitates Zn nucleation. The initial nucleation phase is crucial as it determines the number of active sites and the nucleation density, significantly influencing subsequent Zn growth. As the electrochemical reaction proceeds, metallic Zn continues to grow on the active nucleation areas, forming the metallic deposited layer. However, the surface of commercial Zn foil is typically not atomically smooth, and its protrusions can lead to localized electric field enhancements, which attract concentrated nucleation. This uneven nucleation further intensifies the electric field, prompting Zn^{2+} to continue depositing and forming Zn dendrites[9]. It is clear that the formation of Zn dendrites is a complex process influenced by both the electric field and ion concentration. Addressing these challenges is crucial for improving the cycle stability and commercial potential of ZIBs.

In the pursuit of dendrite-free Zn anodes, researchers are actively exploring strategies in coating design [10–11], electrolyte formulation [1,12], and current collector engineering[13]. These efforts aim to enhance the dynamics of ion diffusion, expand the electrode surface area, and shield electrostatic field concentrations, all of which contribute to a more uniform distribution of electric fields and ion concentrations. This uniformity is essential for achieving dendrite-free Zn deposition and, consequently, more stable ZIBs. The development of three-dimensional (3D) current collectors stands out as a promising approach to this end. These 3D collectors can effectively manage the electric fields and ion concentrations, which is instrumental in promoting dendrite-free Zn deposition[14–16]. The larger surface area of 3D electrodes not only mitigates local current density and nucleation overpotential but also provides an abundance of nucleation sites that facilitate uniform Zn deposition[17–18]. Moreover, the 3D electrodes featured with porous structure ensures a uniform distribution of electrolyte, which is conducive to even Zn deposition [19–20].

Examples of current 3D current collectors include commercial 3D copper meshes [21], Zn foam [22], self-assembled

[1] *State Key Laboratory of Polymer Materials Engineering, Polymer Research Institute, Sichuan University, Chengdu 610065, China*

[2] *Guangxi Key Laboratory of Low Carbon Energy Materials, School of Chemistry and Pharmaceutical Sciences, Guangxi Normal University, Guilin 541004, China*

* Corresponding author, E-mail: hanna@scu.edu.cn (H. He); chuhong.zhang@scu.edu.cn (C. Zhang)

Received 28 October 2024; Accepted 25 November 2024; Published online

DOI: 10.54227/mlab.20240007

graphene aerogels [23], and 3D-printed grid nickel [24]. However, the complex fabrication processes involved in creating most 3D Zn anodes can make them challenging to regulate effectively. The irregular topological structures can significantly affect the distribution of electric fields and the sites of ion deposition on the electrodes. 3D printing technology offers a cutting-edge solution to these challenges. By allowing for the layer-by-layer construction of materials, it enables the creation of intricate 3D structures that traditional manufacturing methods cannot achieve[25–27]. This technology has been increasingly utilized in the production of electrochemical energy storage devices[28–30]. Despite this, the majority of 3D-printed electrodes feature lattice or interdigitated structures, and the specific impact of different topological designs on electrochemical performance remains an area ripe for further investigation.

Herein, we utilized 3D printing technology to engineer a 3D anode with an optimized topological structure, which establishes a uniform electric and ionic flux, leading to dendrite-free Zn deposition. Initially, we investigated the impact of different topological structures (hexagonal, square, triangular, and array) on Zn deposition behavior. Furthermore, we performed theoretical calculations to simulate the ion distribution within Zn anodes featuring different 3D topological structures. These calculations confirmed that the array structure, particularly on the 3DP-180 anode with few electrode joint points can facilitate a more uniform electric field by mitigating the tip effect. The uniform electric field characteristic of the array structure is instrumental in reducing nucleation overpotential, which in turn promotes uniform ion diffusion and prevents dendrite formation. Consequently, the 3DP-180||3DP-180 symmetrical cell demonstrated a remarkable cycling lifespan of 800 hours at a current density of 1 mA cm^{-2} and a capacity of 0.5 mAh cm^{-2}. This achievement underscores the significance of customized structural design in creating a dendrite-free Zn anode, which is pivotal for the development of next-generation durable ZIBs.

Materials and methods

The preparation of 3D-printed Zn anodes

2 g cellulose triacetate (Aladdin Co. Ltd.) was added and dispersed in 20 mL N-methyl-2-pyrrolidone (NMP, Shanghai Aladdin Biochemical Technology Co., Ltd) using a high-speed disperser (T25, IKA Company) for 120 minutes. Then, 0.6 g of carbon nanotubes (CNT, Nanjing XFNANO Materials Tech Co., Ltd), 0.4 g of graphene (Shanghai Aladdin Biochemical Technology Co., Ltd.) and 16 g of Zn powder (Zhongkewanda Company) were added, and the dispersion continued for 2 hours to obtain a uniform ink. The uniformly-dispersed ink was loaded into a syringe and 3D printed using a 3D printer (Allevi 3, Allevi Company) according to single-layer structures, including equilateral triangle, square, hexagon, and linear shapes with angles of 60°, 90°, 120°, and 180°, respectively. The diameter of the printing nozzle was ~600 μm and the printing speed was of 40 mm s^{-1}. After 3D printing, the samples were subjected to solvent exchange in deionized water for 1 hour. Subsequently, they are freeze-dried for 24 hours to obtain the 3D Zn anodes.

The preparation of KVO cathodes

The hydrothermal method was used to prepare the cathode, where 0.115 g of potassium citrate was added was added to 10 mL of water and stirred for 30 minutes, and then, 0.18 g of vanadium pentoxide was added and stirred for 30 minutes. The raw materials for the cathodes were purchased from Shanghai Aladdin Biochemical Technology Co., Ltd. The resulting solution was transferred to a hydrothermal reactor and heated at 200 °C for 24 hours. After the freeze-drying process, the potassium vanadate (KVO) powder was obtained as the active materials. The cathode was prepared by adding the active material, conductive carbon black, and binder PVDF in a mass ratio of 8:1:1 into 1 mL NMP. After dispersion, the slurry was uniformly coated on a 1 cm × 1 cm titanium foil and went through a drying process in a 70 °C convection oven for 24 hours to obtain the KVO cathode.

Characterization

The morphologies of 3D anodes were characterized by the scanning electron microscopy (SEM, Quanta, FEI Company). The X-ray diffraction (XRD, Smart Lab III, Japan Rigaku Instrument Co., LTD) were characterized to analysis material phase with a scan rate of 5° min^{-1}. The rotational rheometer (AR2000, TA Company) was adopted to characterize the rheological properties of ink, where storage/loss modulus and the viscosity of the ink were obtained at room temperature and the gap between the rotational plate and pedestal was 1 mm. COMSOL Multiphysical software was used to simulating the ion concentration during the deposition process.

Electrochemical performance

The electrochemical performance of the half-cell and symmetrical cell was investigated on a CT2001A battery test system (Wuhan LAND Electronic Co., Ltd.). The half-cell test was carried out on the Cu||3D anode configuration with a current density of 1 mA cm^{-2} and a cut-off voltage of 0.5 V. Two pieces of Zn anodes were used to form a coin symmetrical cell configuration with 3M $(CF_3SO_3)_2Zn$ as the electrolyte. The current density was 1 mA cm^{-2} and the capacity was 0.5 mA cm^{-2}. As for the full-cell test, the cyclic voltammetry curves were obtained on the VMP3 multichannel electrochemical workstation (Bio-logic Company) while the charge-discharge curves were obtained from the CT2001A battery test system.

Results and discussions

The fabrication process of 3D-printed Zn anodes primarily involves three main processes, including ink dispersion, performing 3D printing, and completing the solvent exchange. As depicted in Fig. 1a, Zn powder, carbon nanotubes (CNT), graphene, triacetate cellulose nanofiber (TCNF), and N-methyl-2-pyrrolidone (NMP) were mixed and dispersed to form an ink for smooth 3D printing. To print different 3D structures, various 3D models are initially constructed with 3DMax software. After 3D printing, the 3D Zn anodes were placed in deionized water for a solvent exchange and followed by a freeze-drying process. The rheological properties of the ink are the key factors influencing the ink's flow and deformation during 3D printing. The viscosity of ink not only impacts the flow rate but also affects the uniformity of ink extrusion, which subsequently affects the performance of the prin-

DOI: 10.54227/mlab.20240007

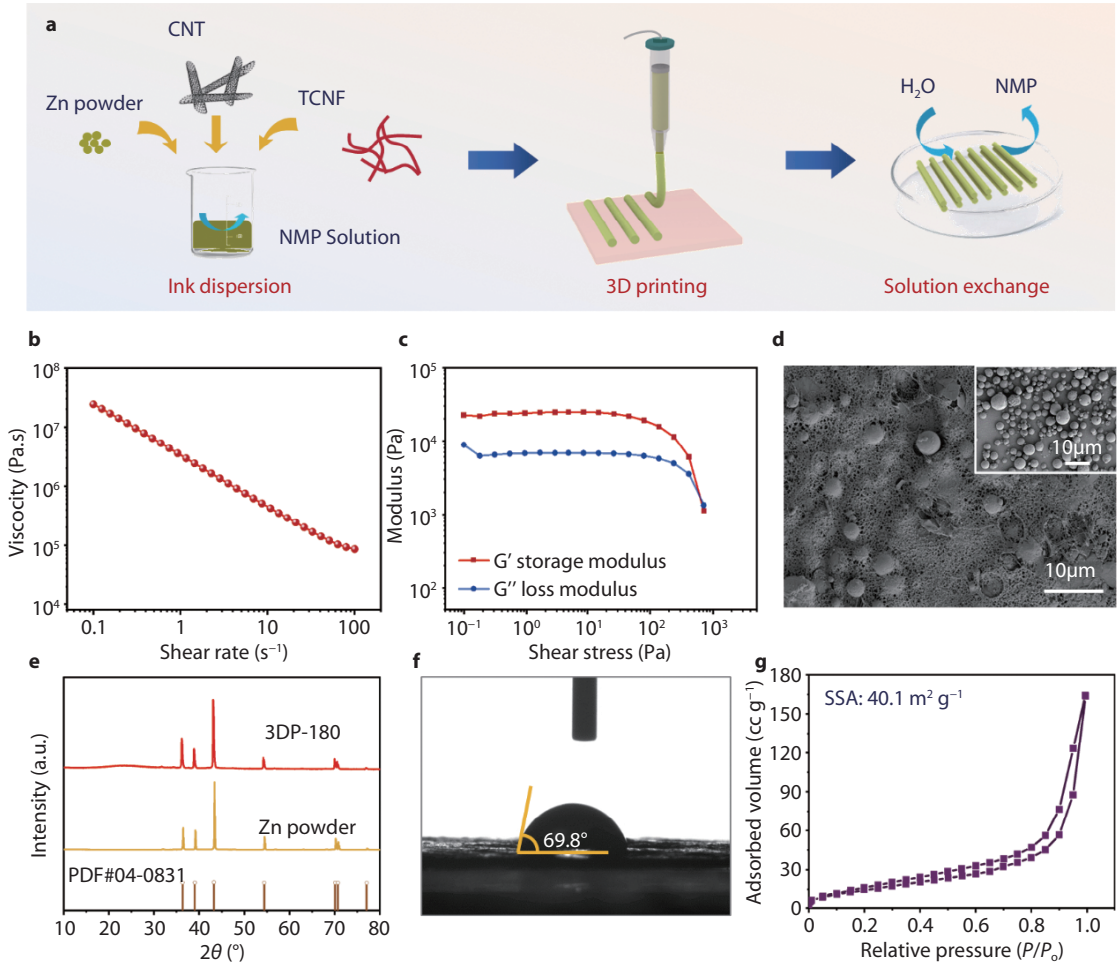

Fig. 1 **a** The schematic illustration of the preparation process of 3D anodes. **b** Viscosity and **c** the modulus curves of the printable ink. **d** The SEM image of 3D Zn anode; inset: the SEM image of the pristine Zn powder. **e** The XRD pattern of the 3DP-180 anode and pristine Zn powder. **f** The contact angle of the 3DP-180 anode. **g** The N_2 absorption/desorption isotherm of the 3DP-180 anode.

ted electrode. A rotational rheometer was employed to analyze the rheological properties of the ink. As shown in Fig. 1b, the viscosity decreases as the shear rate increases, indicating the favorable shear-thinning characteristics of print ink. Moreover, as shown in Fig. 1c, the modulus curve reveals that when the shear stress is less than the yield stress (approximately 1000 Pa), the greater storage modulus than the loss modulus suggests that the printed electrode tends to be an elastic solid with excellent shape retention and mechanical stability after being extruded from the 3D printing nozzle [31]. When the shear stress exceeds the yield stress, the storage modulus of the ink is less than the loss modulus, indicating that when the shear stress applied is greater than 1000 Pa, the ink transforms into elastic liquid. Hence, a printing pressure above 1000 Pa can realized the fluent ink extrusion. Furthermore, SEM images of pure Zn powder and Zn anode are presented in Fig. 1d. It can be observed that the pristine Zn powder with a diameter of ~5 μm is evenly distributed within the Zn anode and tightly wrapped by a 3D network structure constructed by TCNF and CNT, ensuring good electronic conductivity of the electrode and preventing detachment from the electrode during the repetitive plating/stripping processes. As the XRD patterns displayed inFig. 1e, the 3DP-180 anode shows the same typical peaks with the Zn powder that accord well with Zn (PDF#04-0831), revealing the stability of Zn powder during the printing process. The contact angel of the 3DP-180 anode is shown in Fig. 1f, where the anode delivers good wettability of electrolyte with a contact angel of 69.8°. In addition, as the N_2 absorption/desorption isotherm shown in Fig. 1g, the 3DP-180 anode delivers a high surface area of 40.1 m^2 g^{-1}, which insures the sufficient ion diffusion for uniform Zn deposition.

By programming the 3D printer with specific instructions, four anodes with unique topologic configurations, including hexagonal, square, triangular, and array structures were constructed. The angles formed between adjacent printed filaments for these anodes were 60°, 90°, 120°, and 180°, respectively. Correspondingly, the resulting 3D-printed Zn electrodes were designated as 3DP-60, 3DP-90, 3DP-120, and 3DP-180. Fig. 2a-d shows the surface morphology of the Zn anodes, where the surfaces of these 3D-printed anodes exhibit a generally smooth texture. Elemental mapping images, as depicted in Fig. 2, reveal the uniform distribution of Zn and C elements across the electrode surface regardless of their topologic configurations. The Zn elements were derived from the introduced Zn powder, while the C elements were primar-

DOI: 10.54227/mlab.20240007

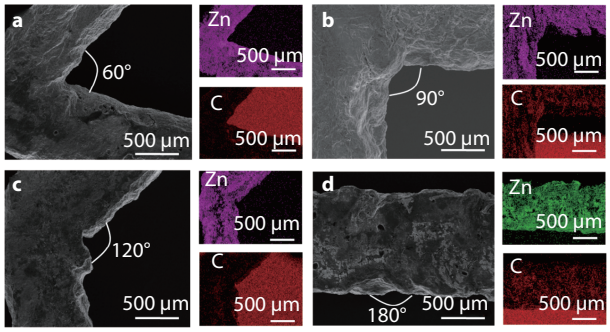

Fig. 2 The SEM images and corresponding element mapping of these four different Zn anodes.

ily attributed to the carbon matrix. This uniformity ensures the intertwined conductive networks within the electrode.

Utilizing the COMSOL Multiphysics simulation software, the Zn deposition process on four distinctively shaped Zn anodes was meticulously simulated. As illustrated in Fig. 3, the joint points formed by the adjacent printed filaments decreased with the increased angles. In 3DP-60 electrode, which featured with the most joint points within the anode, Zn^{2+} predominantly accumulated at the joint points within a deposition time of 30 seconds. Prolonging the deposition time intensified the ion concentration disparity between the joints and the plat areas of the electrode. Upon reaching a deposition time of 100 seconds, the joint ion concentration of 3DP-60 electrode peaked at 2000 mol m^{-3}, resulting in a markedly non-uniform distribution across the electrode surface, which is detrimental to the uniform deposition of Zn^{2+}. However, it is observed that an increase in the angle between adjacent printed filaments led to a more uniform ion concentration distribution on the 3DP-90, 3DP-120, and 3DP-180 electrodes. Notably, the Zn^{2+} concentration exhibited the most uniform distribution on the 3DP-180 electrode with an array topological structure, and this uniformity was sustained with increased deposition time. At the 100s mark, the ion concentration on the 3DP-180 electrode consistently maintained at 1600 mol m^{-3}. The simulation outcomes suggest that ion concentration distribution within the anode becomes increasingly uniform as the joint points decrease. This uniformity was more favorable for the even Zn deposition and the mitigation of Zn dendrite growth. The simulation point to the 3DP-180 electrode, with its array topological structure, as the most effective configuration for achieving a uniform distribution of Zn^{2+}. This optimal distribution is instrumental in suppressing Zn dendrite growth, thereby enhancing the cycling performance of batteries.

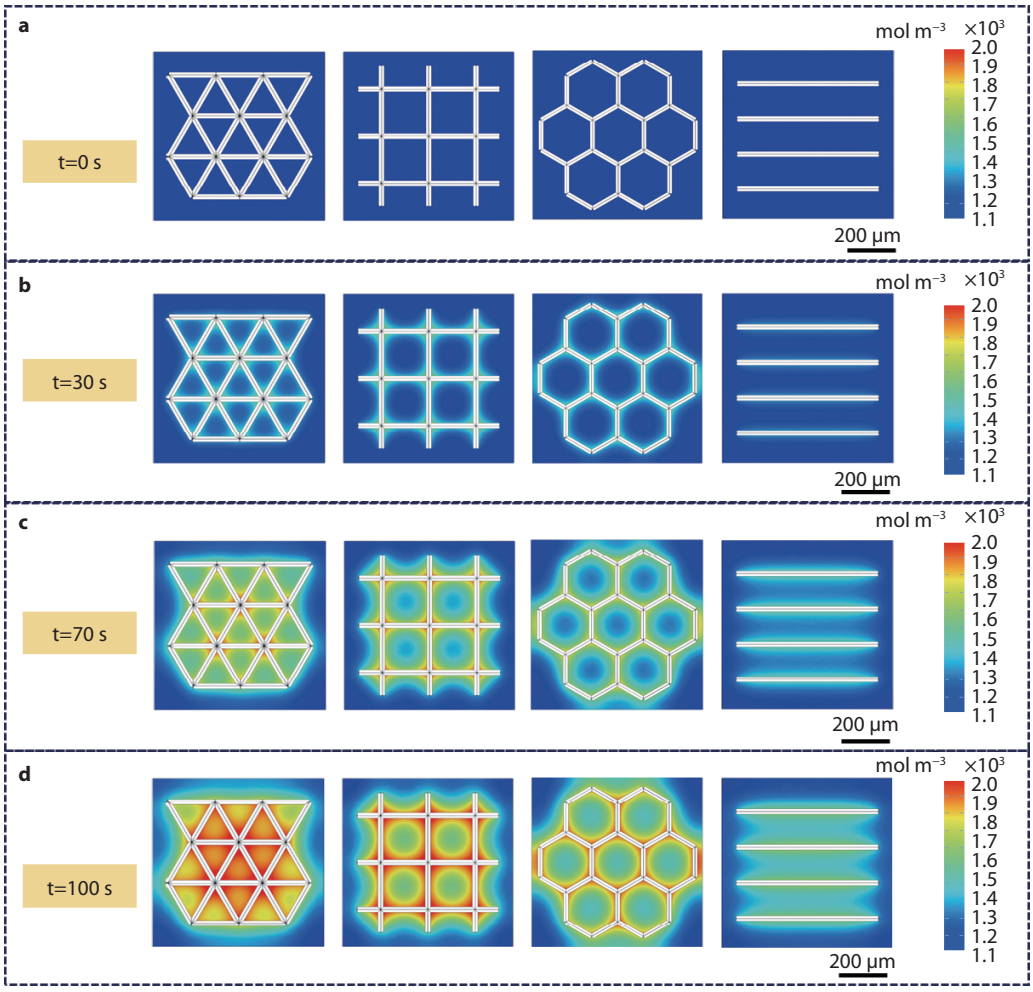

Fig. 3 The COMSOL multiphysics simulation of Zn deposition on 3D Zn anodes with different topological structures.

DOI: 10.54227/mlab.20240007

A coin-type half-cell was assembled using a copper foil as the cathode and 3D-printed 3D Zn anodes of different topological structures as the anode, with 3M $Zn(TFO)_2$ as the electrolyte and a cellulose membrane as the separator. The test current density was 1 mA cm^{-2}, and the cut-off charging voltage was 0.5 V. Fig. 4a displays the nucleation overpotential of the Zn deposition process for these 3D Zn anodes, where the nucleation overpotential of 3DP-180 anode was only 27.2 mV. As the angle between two adjacent filaments decreased, the nucleation overpotential gradually increased, with 3DP-60 reaching an overpotential of 101.6 mV. The smaller the nucleation overpotential, the easier it is for Zn^{2+} to nucleate, and the more uniform the Zn deposition [32–34]. Through potential analysis of the half-cell, it can be found that 3DP-180 anode with few electrode joint points is most conducive to suppressing dendrite growth. The Coulombic Efficiency (CE) during the Zn deposition/stripping process was further conducted and the results are showed in Fig. 4b. The low CE at the beginning of the charge-discharge cycling is possibly due to the large specific surface area of the electrode. During subsequent plating/stripping processes, as the electrolyte fully wetted the electrode, the CE approached 100% after 100 charge/discharge cycles, indicating that the highly reversible Zn plating/stripping behavior, which offers superior lifespan and durability in practical applications. Simulation of Zn deposition and half-cell performance testing confirmed that the 3DP-180 electrode possessed a more uniform ion concentration distribution and lower nucleation overpotential, which essentially determined that the 3DP-180 anode with the optimal performance is most likely to achieve a dendrite-free Zn anode.

A 3DP-180||3DP-180 symmetrical cell was assembled using 3DP-180 as both the cathode and anode. Fig. 4c shows that the 3DP-180||3DP-180 symmetrical cell exhibits a good cycling stability and reversibility within 800 hours at a current density of 1 mA cm^{-2} and a limited capacity of 0.5 mAh cm^{-2}. Additionally, the polarization voltage of the symmetric cell remains stable at below 0.1 V, indicating that the battery operates stably without short-circuit.

To further investigate the performance of 3DP-180 in practical applications, a full aqueous ZIB was assembled using 3DP-180 as the anode and potassium vanadate (KVO) as the cathode. The electrolyte was 3M $Zn(TFO)_2$, and the separator is the cellulose membrane. As the SEM image shows in Fig. 5a, the KVO cathode deliver the obvious band shaped. Meanwhile, the XRD result in Fig. 5b demonstrates the successful preparation of the KVO cathode, where the typical peaks correspond well with the standard $K_{0.486}V_2O_5$ (JCPDS No. 86–0347) [35]. Fig. 5c presents the cyclic voltammetry (CV) curves of the KVO//3DP-180 full cell within a voltage range of 0.2-1.6 V at a scanning rate of 0.1 mV s^{-1}. It can be observed that the CV curves exhibit five typical redox peaks of KVO, and the peak heights of each oxidation peak and reduction peak are close, indicating the excellent reversibility of the redox reactions on the electrode surface, which is conducive to extending the lifespan of the battery [35–36]. Fig. 5d illustrates the charge/discharge curves of the KVO//3DP-180 full cell at a current density of 0.1 A g^{-1}, where the full cell shows obvious oxidation/reduction platforms and delivers a high discharge capacity of 325.8 mAh g^{-1}. As the rate performance shows in

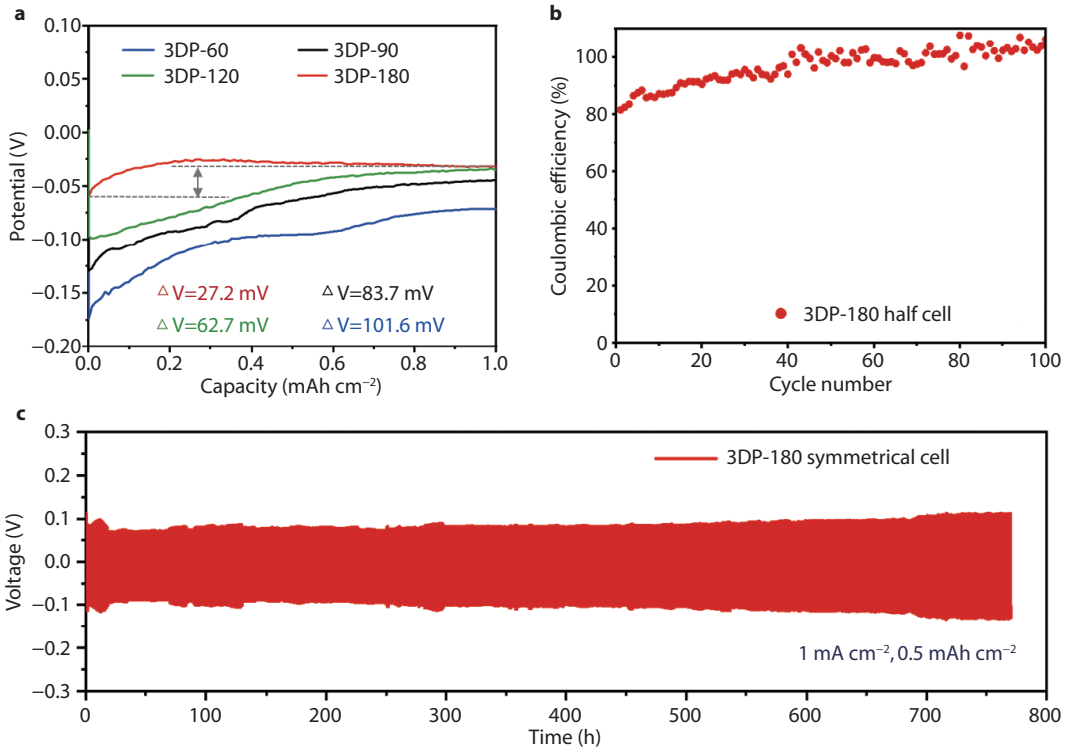

Fig. 4 **a** The voltage curve of the half-cells assembled with different 3D Zn anodes; **b** The coulombic efficiency of the 3DP-180 half-cell; **c** The cycling performance of the 3DP-180||3DP-180 symmetrical cell.

DOI: 10.54227/mlab.20240007

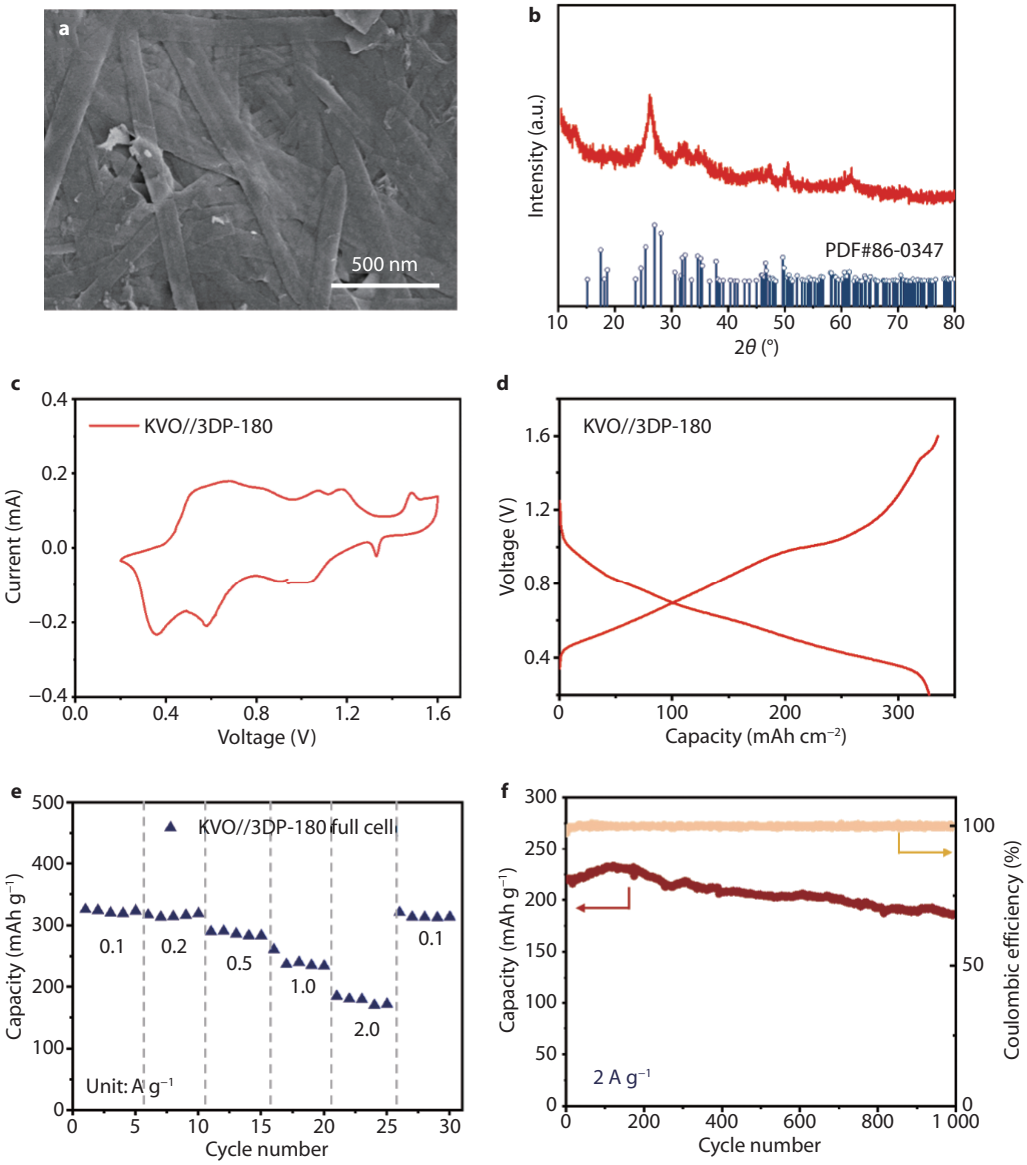

Fig. 5 **a** The SEM image of KVO cathode; **b** The XRD spectrum of KVO cathode; **c** The cyclic voltammetry curve of KVO||3DP-180 full cell; **d** the charge-discharge curves of KVO||3DP-180 full cell at 0.1 A g^{-1}; **e** The rate performance and **f** the cycling lifespan of KVO||3DP-180 full cell.

Fig. 5e, the KVO//3DP-180 full cell demonstrates a capacity of 317.0 mAh g^{-1}, 290.8 mAh g^{-1} and 261.2 mAh g^{-1} with current density varied from 0.2 A g^{-1} to 1.0 A g^{-1}, respectively. Furthermore, upon reducing the current density back to 0.1 A g^{-1}, the discharge capacity impressively recovers to 321.1 mAh g^{-1}, a value that is nearly identical to its initial capacity. This recovery indicates a high degree of reversibility and stability of the ZIB. In addition to the rate performance, the long-term cycling stability of the KVO//3DP-180 full cell was also evaluated at a high current density of 2.0 A g^{-1}. The cell also exhibited exceptional endurance by maintaining a high capacity of 185.7 mAh g^{-1} even after 1000 cycles with CE close to 100% (Fig. 5f). These outstanding results in both rate performance and cycling stability are attributed to the optimized structural design of the Zn anode, which plays a crucial role in enhancing the overall performance of the KVO//3DP-180 full cell.

Summary and outlook

In summary, four Zn anodes with different distinct topological configurations were constructed through the advanced 3D printing technology. Among them, the 3D array 3DP-180 anode with a 180° angle between connected printing strips exhibited fewer joint points led to a more uniform electric field. This uniformity facilitated even ion distribution and significantly suppressed the formation of Zn dendrites. The 3DP-180 array anode showcased an impressively low nucleation overpotential of only 27.2 mV, demonstrating an enhanced capability for Zn nucleation and consistent Zn deposition. Furthermore, a symmetrical cell equipped with the 3DP-180 array anode sustained 800 hours of stable cycling without performance decline at 1 mA cm^{-2} and 0.5 mAh cm^{-2}. These findings underscore the substantial benefits of the optimized 3D structural design of durable Zn anodes in high-performance ZIBs.

DOI: 10.54227/mlab.20240007

■ ACKNOWLEDGMENTS

This work was financially supported by the National Natural Science Foundation of China (No. 51933007, No. 52273250, No. 52373047, No. 523B2036), the Sichuan Youth Science and Technology Innovation Research Team Project (No. 2022JDTD0012), the Program for Featured Directions of Engineering Multidisciplines of Sichuan University (No.2020SCUNG203), the State Key Laboratory of Polymer Materials Engineering (No. sklpme-2023-1-03), the Guangxi Key Laboratory of Low Carbon Energy Materias (2024GXKLLCEM0102).

■ DECLARATION OF INTEREST STATEMENT

The authors declare that they have no known competing financial interests or personal relationships that could have appeared to influence the work reported in this paper.

■ AUTHOR CONTRIBUTION

L. Zeng conceived the idea and wrote the paper. Y. Fang synthesized and characterized the samples, and analyzed the results. D. Luo and D. Du characterized the electrochemical performance. S. Hu, H. He, and C. Zhang discussed and commented on the manuscript.

■ REFERENCES

1. R. Chen, W. Zhang, Q. Huang, C. Guan, W. Zong, Y. Dai, Z. Du, Z. Zhang, J. Li, F. Guo, *Nano-Micro Letters*, 2023, 15, 81
2. J. Bae, S. Oh, B. Lee, C. H. Lee, J. Chung, J. Kim, S. Jo, S. Seo, J. Lim, S. Chung, *Energy Storage Materials*, 2023, 57, 277
3. Y. Mei, J. Zhou, B. Zhang, L. Li, F. Wu, Y. Huang, R. Chen, *SusMat*, 2024, 4, e197
4. J. Hao, L. Yuan, Y. Zhu, M. Jaroniec, S. Z. Qiao, *Advanced Materials*, 2022, 34, 2206963
5. X. Wang, C. Sun, Z. S. Wu, *SusMat*, 2023, 3, 180
6. L. Zeng, H. He, H. Chen, D. Luo, J. He, C. Zhang, *Advanced Energy Materials*, 2022, 12, 2103708
7. M. Zhu, Q. Ran, H. Huang, Y. Xie, M. Zhong, G. Lu, F.-Q. Bai, X.-Y. Lang, X. Jia, D. Chao, *Nano-Micro Letters*, 2022, 14, 219
8. X. Long, Y. Liu, D. Wang, Y. Nie, X. Lai, D. Luo, X. Wang, *Journal of Materials Chemistry A*, 2024, 12, 13181
9. L. Zeng, J. He, C. Yang, D. Luo, H. Yu, H. He, C. Zhang, *Energy Storage Materials*, 2023, 54, 469
10. F. Tao, Y. Liu, X. Ren, J. Wang, Y. Zhou, Y. Miao, F. Ren, S. Wei, J. Ma, *Journal of Energy Chemistry*, 2022, 66, 397
11. J. Zheng, Z. Huang, F. Ming, Y. Zeng, B. Wei, Q. Jiang, Z. Qi, Z. Wang, H. Liang, *Small*, 2022, 18, 2200006
12. A. Naveed, H. Yang, Y. Shao, J. Yang, N. Yanna, J. Liu, S. Shi, L. Zhang, A. Ye, B. He, *Advanced Materials*, 2019, 31, 1900668
13. W. Wang, Y. C. Lu, *SusMat*, 2023, 3, 146
14. H. He, L. Zeng, D. Luo, J. He, X. Li, Z. Guo, C. Zhang, *Advanced Materials*, 2023, 35, 2211498
15. N. Guo, W. Huo, X. Dong, Z. Sun, Y. Lu, X. Wu, L. Dai, L. Wang, H. Lin, H. Liu, *Small Methods*, 2022, 6, 2200597
16. Y. Mu, Z. Li, B.-k. Wu, H. Huang, F. Wu, Y. Chu, L. Zou, M. Yang, J. He, L. Ye, *Nature Communications*, 2023, 14, 4205
17. Y. Du, X. Chi, J. Huang, Q. Qiu, Y. Liu, *Journal of Power Sources*, 2020, 479, 228808
18. X. Fan, H. Yang, X. Wang, J. Han, Y. Wu, L. Gou, D. L. Li, Y. L. Ding, *Advanced Materials Interfaces*, 2021, 8, 2002184
19. Z. Kang, C. Wu, L. Dong, W. Liu, J. Mou, J. Zhang, Z. Chang, B. Jiang, G. Wang, F. Kang, *ACS Sustainable Chemistry & Engineering*, 2019, 7, 3364
20. M. Zhang, Y. Su, G. Li, B. Tang, S. Zhou, X. Wang, D. Liu, G. Zhu, *Journal of Power Sources*, 2024, 589, 233755
21. Q. Zhang, J. Luan, L. Fu, S. Wu, Y. Tang, X. Ji, H. Wang, *Angewandte Chemie International Edition*, 2019, 58, 15841
22. X. Wu, Z. Yang, Q. Song, X. Sun, Y. Xu, M. Zhao, X. Li, Y. Yan, M. Chen, *Chemical Engineering Journal*, 2024, 497, 154395
23. J. Zhou, M. Xie, F. Wu, Y. Mei, Y. Hao, L. Li, R. Chen, *Advanced Materials*, 2022, 34, 2106897
24. G. Zhang, X. Zhang, H. Liu, J. Li, Y. Chen, H. Duan, *Advanced Energy Materials*, 2021, 11, 2003927
25. W. Kang, L. Zeng, S. Ling, C. Zhang, *Advanced Energy Materials*, 2021, 11, 2100020
26. T. Chu, S. Park, K. Fu, *Carbon Energy*, 2021, 3, 424
27. Y. Chang, Q. Cao, B. J. Venton, *Current opinion in electrochemistry*, 2023, 38, 101228
28. J. Wang, Q. Sun, X. Gao, C. Wang, W. Li, F. B. Holness, M. Zheng, R. Li, A. D. Price, X. Sun, *ACS applied materials & interfaces*, 2018, 10, 39794
29. L. Zeng, S. Ling, D. Du, H. He, X. Li, C. Zhang, *Advanced Science*, 2023, 10, 2303716
30. C. Sun, S. Liu, X. Shi, C. Lai, J. Liang, Y. Chen, *Chemical Engineering Journal*, 2020, 381, 122641
31. G. Zhu, H. Zhang, J. Lu, Y. Hou, P. Liu, S. Dong, H. Pang, Y. Zhang, *Advanced Functional Materials*, 2024, 34, 2305550
32. X. Wang, G. Ding, Z. Ma, Z. Xu, Y. Feng, W. Gong, C. Liu, K. Tian, Z. Yong, Q. Li, *Chemical Engineering Journal*, 2023, 472, 144996
33. S. Jiao, J. Fu, M. Wu, T. Hua, H. Hu, *ACS nano*, 2022, 16, 1013
34. J. Hao, S. Zhang, H. Wu, L. Yuan, K. Davey, S. Qiao, *Chemical Society Reviews*, 2024, 53, 4312
35. Q. Deng, Z. Zhao, Y. Wang, R. Wang, J. Wang, H. Zhang, L. Feng, R. Yang, *ACS Applied Materials & Interfaces*, 2022, 14, 14243
36. J. Hao, L. Yuan, Y. Zhu, X. Bai, C. Ye, Y. Jiao, S. Qiao, *Angewandte Chemie International Edition*, 2023, 62, e202310284